International Journal of Heat and Mass Transfer 192 (2022) 122763

Contents lists available at ScienceDirect

International Journal of Heat and Mass Transfer

journal homepage: www.elsevier.com/locate/hmt

Design and performance of a variable gap system for thermal conductivity measurements of high temperature, corrosive, and reactive fluids[☆]

Ryan C. Gallagher[a,b,*], Anthony Birri[a], Nick Russell[a], N. Dianne B. Ezell[a]

[a] *Oak Ridge National Laboratory, 1 Bethel Valley Rd, Oak Ridge, TN 37830, United States of America*
[b] *Department of Nuclear Engineering, The Ohio State University, 201 W 19th Ave, Columbus, OH 43210, United states of America*

ARTICLE INFO

Article history:
Received 7 January 2022
Revised 26 February 2022
Accepted 4 March 2022
Available online 23 April 2022

Keywords:
Thermal conductivity
Fluid properties
Property characterization
Molten salt
Heat transfer
Energy materials

ABSTRACT

High-temperature fluids such as molten salts, liquid metals, and gasses are being proposed for many advanced energy systems including thermal energy storage devices, concentrating solar plants, and advanced nuclear reactor designs. However, the chemical behavior and thermophysical properties of many of these fluids have not been well characterized, which hinders the design, modeling, safety analysis, and deployment of these systems. Thermal conductivity is a property that is especially limited by existing measurement capabilities, which are subject to errors caused by convection, material interaction, radiative heat transfer, and instrument degradation. Therefore, there is a lack of standard, systematic measurement techniques for high-temperature, reactive, and corrosive fluids. In this work, the development of a variable gap thermal conductivity measurement system is detailed. The system is designed to measure the thermal conductivity of highly corrosive and reactive fluids, and survive operation between 100 °C and 800 °C. The effects of convection are minimized by limiting the thickness of the specimen to thin sizes ($<$0.3 mm). Corrections for radiative heat transfer were included in the working equations to consider specimens with varying optical properties. The design, construction, instrumentation, operating principles, and data analysis techniques are discussed in detail. The system was tested up to 500 °C using helium gas and molten KNO_3–$NaNO_3$ to verify the measurement technique and determine the sources of error. At 300 and 400 °C KNO_3–$NaNO_3$, results showed maximum relative error of 6% when compared to results in the literature. The helium results were within 13% of those in the literature at 300 and 400 °C. Higher errors were observed at 500 °C for both fluids, and the sources of these errors are discussed.

1. Introduction

Many potential low-carbon energy systems rely on the use of high-temperature heat transfer or heat storage fluids. High-temperature, i.e. above 400 °C, molten salts, for example, have favorable properties for heat transfer and storage [1,2]. Thermal energy storage (TES) and concentrating solar plants (CSP) have already been demonstrated commercially with nitrate-based molten salts and steam [3–8]. However, the efficiency and energy density of TES and CSP systems would be improved by utilizing higher operating temperatures enabled by higher temperature fluids, including molten metals, molten salts, and compressed gasses [5,9–11]. Moreover, some system designs will require even higher temperature fluids, such as energy storage units that have been proposed for integration with industrial processes to recover and repurpose waste heat streams that may have temperatures above 800 °C [12–14]. Nuclear power would also benefit from the utilization of higher temperature fluids to improve safety, efficiency, and potentially reduce the capital cost of nuclear reactors [15]. Higher temperature reactors also enable hybridization with other technologies such as process heat applications, hydrogen production [16], and supercritical CO_2 Brayton cycles [11,17]. Numerous advanced reactor design concepts being pursued will utilize molten salts [15,18], liquid metals [19], or high temperature gasses [20]. Additionally, the use of high-temperature salts and metals have been proposed for use in fusion reactors as thermal blankets [20–23].

[☆] This manuscript has been authored by UT-Battelle, LLC, under contract DE-AC05–00OR22725 with the US Department of Energy (DOE). The US government retains and the publisher, by accepting the article for publication, acknowledges that the US government retains a nonexclusive, paid-up, irrevocable, worldwide license to publish or reproduce the published form of this manuscript, or allow others to do so, for US government purposes. DOE will provide public access to these results of federally sponsored research in accordance with the DOE Public Access Plan (http://energy.gov/downloads/doe-public-access-plan).

[*] Corresponding author.
E-mail address: gallagherrc@ornl.gov (R.C. Gallagher).

https://doi.org/10.1016/j.ijheatmasstransfer.2022.122763
0017-9310/

Modeling and simulation tools are often employed to design and optimize energy systems, through multiphysics and multiscale modeling which require temperature and composition dependent thermophysical property data as inputs [24]. Accurate knowledge of the thermophysical properties is required for accurate design, optimization, and deployment of these systems [25]. Moreover, high-temperature fluids often have challenging chemical characteristics, including reactivity, corrosivity, and volatility. In molten salt reactors, where nuclear fission products will be continually introduced and potentially removed from the liquid fuel, the fluid's chemistry will have temporal and/or operational condition dependent chemistries for which the thermal properties are uncharacterized, and these properties are currently difficult to predict with modern computational tools. These effects can be simulated with predictive thermochemical or thermophysical models coupled with system models, but these models require experimental data to benchmark and refine modeling techniques [24,25].

The efficiency, operational constraints, and safety of these high-temperature systems will depend strongly on the working fluid's thermophysical properties and corresponding uncertainties. Therefore, techniques to improve and optimize thermal properties—such as thermal conductivity or heat capacity—that directly impact charge/discharge rate of latent heat storage systems, are also under investigation. For example, the use of encapsulated phase change materials in conjunction with a heat transfer fluid, or the addition of nanoparticle additives for latent heat storage, have the potential to improve the thermal performance of potential heat transfer fluids [26–29]. However, experimental measurements will be necessary to quantify the effectiveness of these proposed property enhancement techniques.

Despite the level of interest in utilizing high-temperature fluids and the importance of thermal properties to system performance [30], the properties are not well characterized because of the difficulty of performing experimental measurements at high working temperatures with reactive materials [31]. Molten salt thermal conductivity experimental data are especially scarce, and much of the existing data often have high uncertainties and discrepancies between other studies [9,25,32]. These experimental discrepancies are expected to be a result of measurement bias from competing mechanisms of heat transfer (radiation and convection) [32–34]. Multiple theoretical models have been proposed [35–39], and molecular dynamics simulations [39–44] have also been utilized to predict molten salt thermal conductivity, but both require additional experiments for validation. Although numerous techniques—including transient electrically heated sensors, steady-state heat flow, and optically heated techniques—have been developed [31,34], a standardized and repeatable technique applicable for a wide variety of high-temperature fluids has not yet been established.

1.1. Techniques for fluid thermal conductivity measurements

Generally, thermal conductivity measurement techniques are classified into steady-state and transient methods. Reviews on different thermal conductivity measurement techniques are provided in other works [31,45,46]. Here, we briefly discuss the techniques that have been applied to high-temperature fluids such as molten salts. Transient techniques applied to high-temperature fluids include the transient hot wire (THW), laser flash diffusivity, and forced Rayleigh scattering. The primary disadvantage of these techniques is that they are not direct measurements of thermal conductivity, but rather of thermal diffusivity. This necessitates knowledge of the fluid's heat capacity and density to calculate the conductivity. Steady-state techniques include coaxial cylinder and parallel plate (or axial flow) methods. These techniques generally require large sample volumes relative to transient techniques and have been hypothesized to be affected by convective and radiative errors.

THW is an established technique applied to measure the thermal conductivity of liquids, solids, gasses, and powders [47,48]. The technique relies on measuring the transient temperature rise of a thin wire that is resistively heated by a step increase in power while suspended or embedded in a specimen and relating it to the heat diffusion equation [47,49]. The application of the THW method has proven to be reliable for measuring fluids' thermal conductivity. However, for use in high-temperature reactive fluids, the sensors material selection/fabrication is a major technological challenge because of corrosion and the need for passivation when measuring conductive fluids. The sensor and passivation layer must be chemically inert and resistant to thermal expansion stresses. Furthermore, corrections for the sensor geometry and passivation layer thickness must be considered [50–55]. To simplify the data analysis, the solution to the heat equation used for these sensors typically assumes ideal conditions, such as a thin plane source [56] or an infinitely thin wire [47]. Therefore, these techniques must also carefully consider non-ideal conditions such as the size of the wire/sensor and coating that can result in conduction errors, sensor heat capacity effects, and radiative heat transfer. Corrections for these effects often require a priori knowledge of thermal properties, such as specific heat capacity and density of the sample and sensor materials in the experiment. Often it is nontrivial to measure the other properties of high temperature fluids, such as the heat capacity of molten salts [57]. Similar difficulties also exist for other types of transient probes, including the three-omega (3ω) [58] and transient plane source techniques [56,59].

Another common technique that is widely applied to thermal conductivity measurements of high-temperature materials is the laser flash diffusivity technique, which optically heats a planar specimen on one face with a laser pulse or high-power flash lamp while measuring the transient temperature rise through a specimen of known thickness with an infrared detector on the opposite side [60]. This technique has been applied to high-temperature fluids using custom-designed layered crucibles [61–63], but results suggested an errant positive temperature dependence with temperature. This is expected to be due to a lack of corrections for thermal radiation and conduction losses in a three-layer geometry [35,36,38]. Like other transient techniques, the laser flash technique is not a direct measurement of thermal conductivity and can only provide data on the material's thermal diffusivity without additional heat capacity and density data. Crucible design must consider volatility [64] and wetting [65] of the samples, which can lead to corrosion or contamination of the system over time, as well as measurement errors [57].

Forced Rayleigh scattering, described by Nagasaka et al. [66], employs a heating laser split into two beams crossed within a sample volume, generating an interference fringe pattern. The interference pattern generates a sinusoidal temperature pattern within the sample. The heated region of the sample acts as a phase grating on the probing beam. The transient decay of a short, heat-inducing laser pulse obeys the diffusion heat equation, and analysis of the diffracted probing laser is used to measure the thermal diffusivity. This technique has been applied to a variety of pure molten salts [67–69], and data are considered reference quality [34,35]. However, the technique is limited to transparent, glass cells, which are not compatible with some fluids such as fluoride molten salts [70]. Like the other transient techniques, forced Rayleigh scattering requires a priori knowledge of density and heat capacity.

Steady-state methods commonly require the exposure of two ends/sides of a specimen to surfaces held at two different isothermal temperatures, resulting in a temperature gradient through the specimen thickness. The temperature difference and a measurement of the heat flux through the specimen is used to determine the thermal conductivity through approximations of Fourier's law, a simpler working formulation relative to transient techniques. Steady state methods include coaxial cylinder techniques [71–73], comparative techniques [74], and parallel plate techniques [75–79]. Although these methods have the advantage of direct measurement of thermal conductivity and simpler data analysis relative to transient techniques, steady-state techniques generally require larger sample volumes, sensors, and specimen heat sources. Therefore, mitigation of convective and radiative losses is a significant challenge when applying these types of techniques to fluids [34]. This is especially true when studying high-temperature fluids such as molten salts, which tend to have low viscosities and high thermal expansion coefficients which exacerbate the buoyancy-driven flow if temperature gradients in the specimen exist, thereby introducing error into measurements. The temperature sensors must also account for material contact conductance, as well as the thermal conductance of barrier materials if the sensor cannot be placed in direct contact with the specimen. At high temperatures, corrections for radiative heat transfer must also be considered, and effects will depend on the plate material, surface roughness, and the fluid's optical properties [80,81].

The variable gap technique described by Cooke [82,83], developed primarily for the measurement of thermal conductivity of molten salts at Oak Ridge National Laboratory (ORNL), provides a potential solution to thermal resistance effects, buoyancy-driven errors, and radiative heat transfer corrections. The technique was demonstrated for He, Ar, Hg, and H_2O. It was also demonstrated for a 44-49-7 mol% mixture of KNO_3-$NaNO_2$–$NaNO_3$, and the results showed reasonable agreement with other experimentally measured values and semi-empirical theoretical estimations [82,84]. Like parallel plate and axial flow techniques, the variable gap technique measures steady-state temperature differences through a planar specimen but with small sample thicknesses to reduce buoyancy driven flow in the fluids. Based on the thermal power applied to the specimen, a thermal resistance with respect to specimen thickness is measured to determine the thermal conductivity using an approximate solution to Fourier's law. Variation of the gap thickness removes the uncertainty of contact conductance and thermal resistance between the temperature sensors and the specimen being analyzed (further discussion provided in Section 2). It was also proposed that measurement with sufficiently thin specimen gaps has the potential to measure radiatively non-participating (infrared transparent) fluids with radiative corrections to the working equation as well as participating (semi-transparent) fluids with a correction using refractive index and mean absorption coefficients [80,82].

In this work, a modern measurement system based on Cooke's variable gap technique was designed, built, and tested. The variable gap thermal conductivity system employs a thin (<0.3 mm) specimen, small temperature differences through the specimen (~10–15 °C), non-reactive materials of construction, and modern data acquisition and analysis systems. Measures were taken with this design to reduce temperature gradient through the specimen, as well as specimen thickness to reduce the uncertainties that affected previous works applying steady-state techniques on high-temperature fluids. The data acquisition allowed for the application of novel data analysis algorithms to process the data, and modifications to the variable gap working equations were developed using updated models of radiative heat transfer.

2. Theory

The variable gap technique's measurement principle is like other steady-state techniques, which measure and apply a temperature difference through a known thickness of material to determine the thermal conductivity using approximation of Fourier's law of conduction. This arrangement assumes isothermal, infinite parallel plates held at two different temperatures.

2.1. Ideal analysis model

When considering the 1D heat flow between two sides of a plane of material held at two different temperatures, Fourier's law simplifies to

$$q'' = -\kappa \frac{\Delta T}{x} \ldots \quad \rightarrow -\kappa = \frac{Q * x}{A \Delta T}, \tag{1}$$

and the thermal resistance is

$$R_{th} = \frac{x}{\kappa} = \frac{A \Delta T}{Q}, \tag{2}$$

where q'' is the heat flux, κ is the material thermal conductivity, ΔT is the difference in temperature between the two sides, x is the material thickness, A is the cross-sectional area of the surface above the specimen, and Q is the thermal power. Most steady-state measurement techniques use a single specimen thickness and must include corrections for the total thermal resistance of the materials that are in series with the specimen. Contact thermal resistances can also contribute to the measured resistance, biasing the measured thermal conductivity. One method to circumvent the estimated contact conductance and material thermal resistances is to take thermal resistance measurements with varying specimen thicknesses. This enables a direct measurement of the thermal conductivity by isolating the effects of additional thermal resistance [82,83,85]. Considering a geometry with planar material in between upper and lower temperature probes, the thermal resistance is calculated in series (shown in Fig. 1), and the total thermal resistance between the probes is

$$R_{th,total} = \frac{A \Delta T}{Q} = R_{th,upper} + R_{th,lower} + R_{th,s}. \tag{3}$$

In Eq. (3), $R_{th,upper}$ and $R_{th,lower}$ are the thermal resistances above and below the specimen caused by barrier materials and contact interfaces, and $R_{th,s}$ is the thermal resistance through the specimen thickness. The upper and lower resistances are expected to be nearly static or fixed during a measurement. With $R_{th,upper}$ and $R_{th,lower}$ as components of the total fixed resistance ($R_{th,fixed}$),

$$R_{th,fixed} = R_{th,upper} + R_{th,lower}, \tag{4}$$

and the variation of the specimen thickness is the only variable that will influence the total thermal resistance. Substituting Eq. (4) into Eq. (3) and Eq. (2), the thermal conductivity of the specimen (κ_s) can be described as a linear function of x,

$$\frac{A \Delta T}{Q} = \frac{\Delta T}{q''} = \frac{1}{\kappa_s} x + R_{th,fixed}. \tag{5}$$

Maintaining ideal conditions, in practice, is very challenging because of the effects of convection, radiation, and conductive heat losses, which can result in non-isothermal conditions and errors in the measured conductivity. Eq. (5) applies only to opaque specimens that have large optical thicknesses and do not transmit thermal radiation. In the cases of transparent, optically thin, and radiatively participating species, adjustments to the working equation must be made.

2.2. Treatment of radiative heat transfer

All materials constantly emit and absorb thermal radiation consisting of electromagnetic waves or photons. The effects of radiation are often insignificant when operating near room temperature, but correction for radiative heat transfer is essential for measurements at elevated temperatures. Though it is important, these

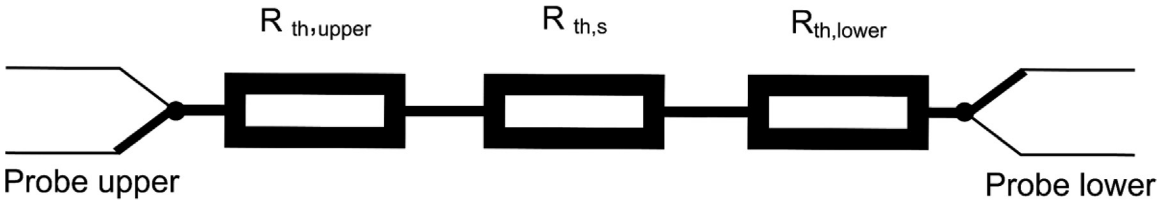

Fig. 1. The resistance network for a planar specimen with material between the temperature reference points (probes).

effects are often poorly quantified because of optical property dependance on many factors including temperature, surface condition of materials, and spectral energy. Like material surface emission and absorption of radiation, a medium can also absorb and emit radiation internally. These materials are referred to as *participating* or *semi-transparent*. When considering the thermal conductivity of semi-transparent materials, especially at elevated temperatures, the apparent enhancement of thermal conductivity due to thermal radiation requires attention [86–90]. Many candidate materials for high-temperature systems including molten salts may refract, absorb, emit, and potentially scatter radiation (in the case of nanoparticle doped fluids, which are not considered herein) [91–94].

It should be noted that numerous techniques with varying complexity exist to solve the radiative heat transfer equation. However, a concise working equation was used in this work that is more tractable to apply with limited knowledge of the specimen's optical properties. In the case of parallel plate instruments, it is reasonable to treat the bounding surfaces as gray, diffuse bodies instead of spectrally dependent surfaces and to make use of approximations that circumvent the requirement of solving the radiation transport equation.

For materials with small optical thicknesses and negligible emission (transparent), the mathematics associated with radiative heat transfer reduce to the Stefan–Boltzmann law of radiation. When a medium is optically thick, such as liquid metals, photons are absorbed, emitted, and reabsorbed without traveling a significant distance within the medium, and radiation can be treated in the same manner as heat conduction, reducing the working equation to Eq. (5).

Transparent, non-emitting specimens like many gasses at moderate temperatures have negligible contributions from thermal radiation. The radiative contribution can be accounted for using the standard expression for radiative heat flux between two gray, diffuse parallel plates held at two different temperatures:

$$q''_{rad} = \frac{\sigma\left(T_1^4 - T_2^4\right)}{\varepsilon_1^{-1} + \varepsilon_2^{-1} - 1}, \text{ or } q''_{rad} = \frac{\varepsilon\sigma\left(T_1^4 - T_2^4\right)}{(2-\varepsilon)} \; \textit{when } \varepsilon_1 = \varepsilon_2, \tag{6}$$

where q''_{rad} is the radiative heat flux, σ is the Stefan–Boltzmann constant, ε is the emissivity of plates 1 or 2, and T is the temperature of plates 1 or 2. Using a thermal resistance network approach, the thermal resistance through the specimen can be expressed assuming parallel resistance, shown in Fig. 2, and the resistance through the specimen is

$$\frac{1}{R_{th,s}} = \frac{1}{R_{th,rad}} + \frac{1}{R_{th,cond}}, \tag{7}$$

where $R_{th,rad}$ and $R_{th,cond}$ are the radiative and conductive resistances.

In Eq. (6), the radiative heat transfer coefficient (h_{rad}) can be used to express q''_{rad} in terms of the temperature difference:

$$q''_{rad} = \frac{\varepsilon\sigma\left(T_1^4 - T_2^4\right)}{(2-\varepsilon)} = h_{rad}(T_1 - T_2). \tag{8}$$

Using Eq. (2), $R_{th,rad}$ can also be described using the radiative heat transfer coefficient:

$$R_{th,rad} = \frac{1}{h_{rad}} = \frac{(2-\varepsilon)}{\varepsilon\sigma(T_1 + T_2)\left(T_1^2 + T_2^2\right)}. \tag{9}$$

Therefore, combining Eq. (9), Eq. (7), the total specimen resistance is

$$\frac{1}{R_{th,s}} = \frac{\varepsilon\sigma(T_1 + T_2)\left(T_1^2 + T_2^2\right)}{(2-\varepsilon)} + \frac{\kappa_s}{x}, \tag{10}$$

and Eq. (5) becomes

$$\frac{\Delta T}{q''} = R_{th,fixed} + \frac{1}{\frac{\varepsilon\sigma x(T_1+T_2)\left(T_1^2+T_2^2\right)}{2-\varepsilon} + \kappa_s} x. \tag{11}$$

Alternatively, the radiative contribution to the effective thermal conductivity can be expressed as κ_{rad}, giving [81]

$$\frac{\Delta T}{q''} = R_{th,fixed} + \frac{1}{\kappa_{rad} + \kappa_s} x. \tag{12}$$

The effects of weakly interacting or semi-transparent fluids when determining the radiative contribution to the thermal conductivity measurement is more complex. Rausch et al. included a correction for radiative participating fluids measured with a guarded parallel plate apparatus [86]. This correction was based on the works of Braun et al. [81], Kohler [95], and Poltz [80]. Cooke [82,83] also described a similar correction for a previous version of a variable gap apparatus. Assuming small temperature differences, a linear temperature distribution through the specimen, and a constant bounding surface emissivity, the κ_{rad} is

$$\kappa_{rad} = \frac{4}{3} c_1 c_2 \int_{\nu=0}^{\infty} n(\nu)^2 \frac{Y(\tau,\varepsilon)}{k(\nu)} \frac{\nu^4 \exp\left(\frac{\nu c_2}{T_{avg}}\right)}{T_{avg}^2\left(\exp\left(\frac{\nu c_2}{T_{avg}}\right) - 1\right)^2} d\nu, \tag{13}$$

where k is the absorption coefficient, ν is the wave number, c_1 and c_2 are the constants in Planck's energy distribution (3.741771×10^{-16} Wm [2] and 1.43877×10^{-2} mK respectively), T_{avg} is the mean specimen temperature, and n is the refractive index. Y, the fluid's reflectance, is a function of the plate emissivity and specimen optical thickness ($\tau = kx$)

$$Y = 1 - \frac{3}{\tau}(2-\varepsilon) \int_0^1 \frac{1 - \exp\left(-\frac{\tau}{\nu}\right)}{1 + (1-\varepsilon)\exp\left(-\frac{\tau}{\nu}\right)} \nu^3 d\nu. \tag{14}$$

From Poltz's tabulation of Y with different values of τ and ε [96], in the case where the optical thickness approaches zero, Y approaches

$$Y = \frac{3}{4}\left(\frac{\varepsilon}{2-\varepsilon}\right). \tag{15}$$

Therefore, treating n independently from the wavelength, Eq. (13) becomes

$$\kappa_{rad} = c_1 c_2 n^2 x \int_{\nu=0}^{\infty} \frac{\nu^4 \exp\left(\frac{\nu c_2}{T_{avg}}\right)}{T_{avg}^2\left(\exp\left(\frac{\nu c_2}{T_{avg}}\right) - 1\right)^2} d\nu. \tag{16}$$

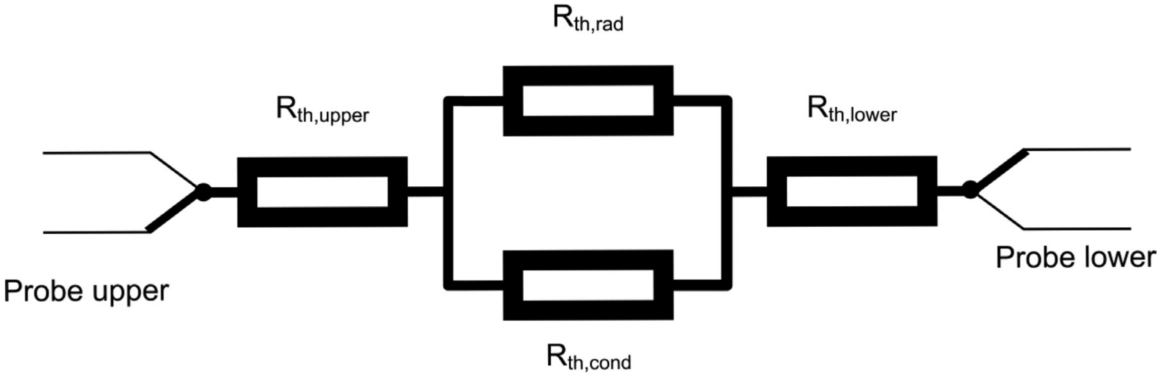

Fig. 2. Resistance network with radiative heat transfer in parallel with conduction.

Eqs. (11), (13), and (16) can be used to analyze participating fluids by modifying κ_{rad} in Eq. (12), depending on the expected optical properties of the specimen being measured.

2.3. Convection effects

Convection effects are considered a primary reason for errors in steady-state measurements of thermal conductivity of high temperature fluids. In this variable gap system, the effects are minimized by heating the specimen with the upper plate and by using a very thin (<0.3 mm) specimen gap. The Rayleigh (*Ra*) number describes the critical value at which buoyancy driven flow becomes significant:

$$Ra = \frac{g\alpha \Delta T x^3 C_p \rho^2}{\kappa \eta}, \tag{16}$$

where g is the gravitational constant, α is the thermal expansion coefficient, C_p is the specific heat capacity, ρ is the density, and η is the dynamic viscosity. As discussed by Rausch et al. [86], a conservative limit to ensure insignificant convection in a parallel plate apparatus is $Ra < 1708$, considering the works of Mostert et al. [97] and Gitterman [98]. This is conservative because the criterion assumes fluid heated from the bottom, instead of from the top. The former having a higher tendency to induce buoyancy driven flows. For this work, the *Ra* of helium was calculated to be well below this criterion for gap sizes below 0.3 mm and temperature differences of 20 °C, which is conservative for this system. The $NaNO_3$—KNO_3 molten salt, however, could approach $Ra > 1708$ at higher temperatures where the viscosity is low. Care was taken to limit the ΔT between the plates and the gap size during these measurements to ensure that natural circulation errors did not affect the measurement. The calculation of *Ra* was completed following measurements using the measured gap size, average temperature, and temperature difference to ensure that convection was negligible.

3. Experiment design and materials

The variable gap thermal conductivity system developed for this work was designed with consideration of the following criteria: (1) standard/simple fabrication and instrumentation consistent with standard production methods; (2) robust design and construction that can withstand continued use at high temperatures (up to 800 °C) and with chemically aggressive specimens; (3) modular construction to allow for rapid replacement of components in the case of damage by corrosion or for improvement and modification of the design; (4) capable of direct measurement of thermal conductivity because other properties, such as density and heat capacity, of the potential fluids may not be well characterized; and (5) compact enough to be loaded and sealed in standard inert glove boxes and fit on a laboratory benchtop.

3.1. Experiment mechanical design

An illustration of the system is shown in Fig. 3. The system consists of a flange-sealed cylindrical chamber, *external containment,* a), which encompasses the specimen, temperature probes, and cooling channels, g). An additional sealed chamber, referred to as the *internal containment,* b), is inserted into the external containment. The internal containment features a welded bellows feedthrough, c), which mates with the top flange of the external containment. The bellows feedthrough enables vertical translation of the internal containment within the external containment while maintaining a hermetic seal between the sample environment and external environment. At the bottom of the internal containment, a cylindrical plate shaped cell—the heating module, d)—contains thermocouples and a mineral-insulated resistive heating element. Axial translation of the internal containment is precisely controlled using a jam-nut coupled to a threaded portion of the internal containment, e). The position of the heater cell relative to the bottom surface of the external containment (gap thickness) is measured with a digital variance indicator, f). The gap thickness during a measurement is generally kept below 0.3 mm when measuring high-temperature fluids to minimize convection effects.

The structure of the system is fabricated primarily from 316 stainless steel for its high-temperature strength and corrosion resistance. The assembled system is small enough to fit in standard glovebox antechambers and seals for transportation, which enables loading and testing of specimens in high-purity, dry, and inert gas environments, among other specific conditions. During operation, the chamber is placed into a tube furnace, which is the primary heating source used to maintain the entire system at the desired equilibrium temperature. The specimen is contained at the bottom of the outer containment; it is cooled on the bottom surface by air cooling channels and heated on the top by the heating module.

An illustration of the specimen-containing region of the apparatus is detailed in Fig. 4, with the key components labeled. The heating module, a), contains the resistive heater, c), which is the main source of heat flux, h), through the specimen, d). The heating module also contains thermocouples to measure the temperature on the top surface of the specimen in the center, e), and on two sides. The heat applied to the top of the specimen results in a temperature difference (ΔT) through its thickness when the specimen is cooled simultaneously by the cooling channels, g), on the bottom surface. The power applied to the top of the specimens is controlled and measured using the current and voltage output of the power supply; the heat flux is calculated using the heater's area.

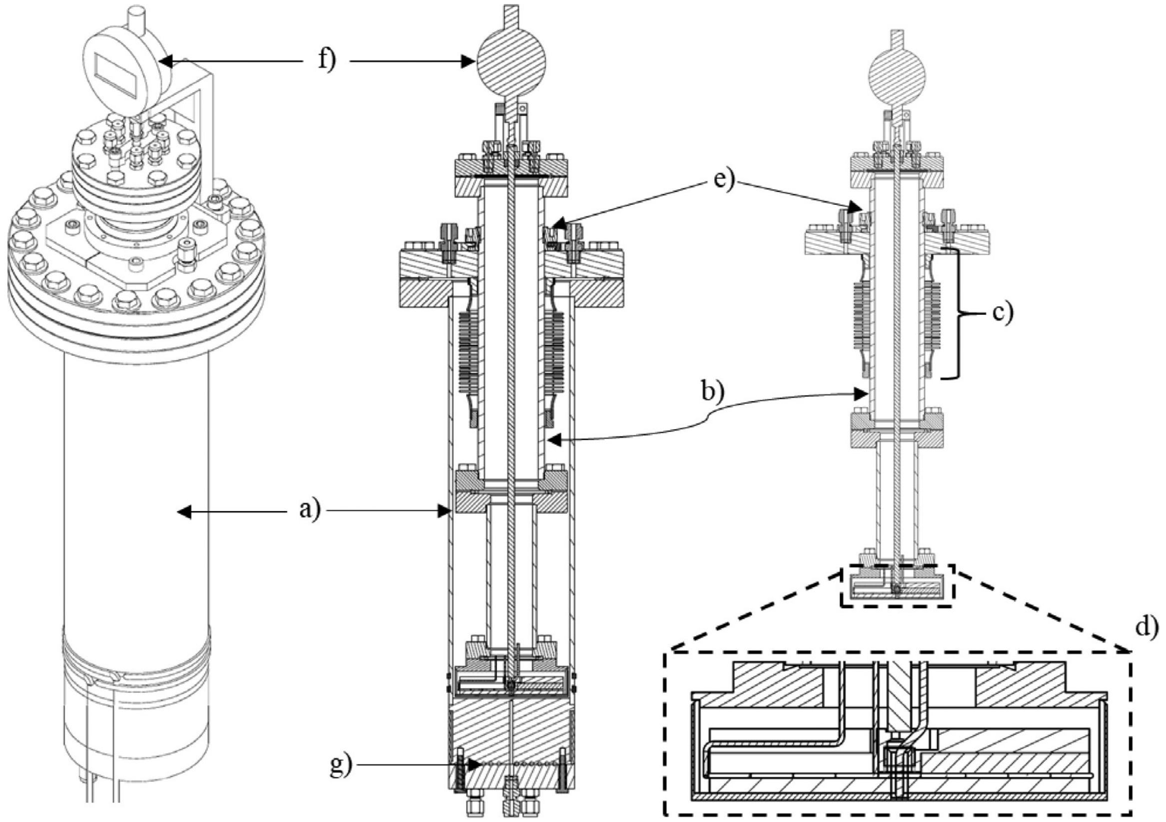

Fig. 3. Schematic and image of the variable gap system: a) external containment, b) internal containment, c) bellows feedthrough, d) heating module, e) jam nut, f) variance indicator, g) cooling channels.

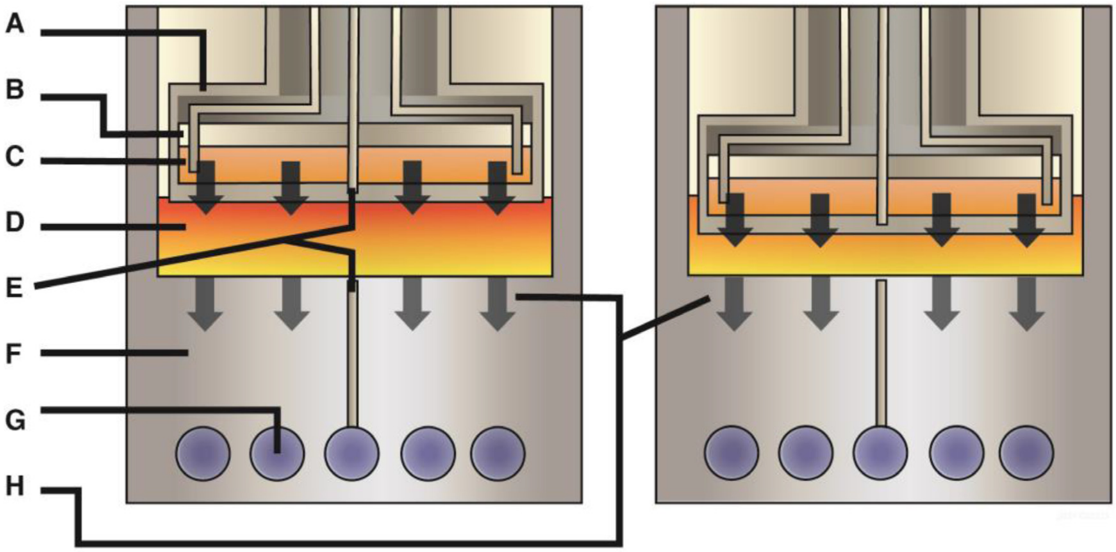

Fig. 4. Depiction of the specimen region of the variable gap thermal conductivity system with a larger (left) and smaller (right) gap. a) heating module, b) insulating disk, c) resistive heater, d) specimen, e) thermocouples, f) external containment chamber, g) cooling channels, h) ideal heat flux vectors.

An insulating quartz disk, b), is located above the heating element to prevent axial heat losses that would bias measurements.

Both the internal and external containments feature gas inlets and valves to remove or supply gas to the system, which can allow for measurement in varying environments, as well as off-gas sampling. Once both chambers are initially filled, with the specimen in place, the pressure is manually controlled to keep the system at the desired pressure during measurements and prevent overpressurization. Although the system is not designed to be pressurized, moderate pressure (103–172 kPa) can be applied to the outer containment to collapse bubbles that may have formed within the fluid gap region during a measurement. This could also be utilized to reduce volatilization of fluids that have moderately high vapor pressures.

It is well known that the emissivity of surfaces is dependent on material, temperature, and the surface roughness. To limit the emissivity, polishing or plating with low-emissivity metals can be performed. In the system used in this work, the bottom surface of the outer containment was mechanically polished to 1.6 rms, whereas the heating plate's bottom surface was further polished with diamond polishing paste down to 0.3 rms. The roughness dependent emissivity of stainless steel was estimated using the expression determined by Taylor et al. with hemispherical directional reflectance [99], and averaged for the two different roughness values used. The emissivity of polished stainless-steel was adjusted for temperature using the classical expression from Davisson and Weeks [100]. Generally, the emissivity ranged from 0.1 to 0.2 for the experimental conditions herein.

3.2. Measurement instrumentation

Two temperature measurements, located near the top (hot) and bottom (cold) sides of the specimen, are required to measure the temperature difference, ΔT, through the gap. In this design, three calibrated N-type thermocouples are positioned inside the heating module. One measures the temperature in the center of the heater, and two measure the temperature on the sides to ensure an isothermal plate temperature. The external containment also features more thermocouples: one near the bottom of the specimen is used for the ΔT measurement through the gap and another located below that, at the cooling channels. All thermocouples were calibrated at the NVLAP-accredited metrology lab at ORNL and had a maximum uncertainty of 0.1 °C. Thermocouples are logged with an Isotech MilliK high-precision thermometer and channel expander, MilliSkanner. The mineral-insulated resistive heater wire is coiled into a disk and sandwiched between two steel plates with a quartz insulating disk above it. A Sorenson XPD120–4.5 DC power supply is used to adjust and record the current and voltage, which is used to calculate the power applied to the top of the specimen. The uncertainties of voltage and current measurements are 0.1 V and 0.001 A, respectively. Cooling by ~0.6 MPa compressed air is monitored using pressure gauges and is adjusted with a needle valve. Lastly, pressure gauges and a gas manifold are attached to the internal and external containment to monitor containment pressure. The gap is measured off the top flange of the internal containment via calibrated digital variance indicator with an accuracy of 0.0025 mm.

3.3. Measurement procedure

After specimens are loaded, the setpoint on the surrounding furnace is set to the desired temperature. Once thermal equilibrium is reached, power is supplied to the resistance heater located above the specimen. The radial temperature profile is monitored during the application of power to the heater to maintain <1 °C difference between the center and sides of the heating cell. This ensures that minimal heat flux is lost/added radially and that the heat flux through the specimen can be accurately calculated. Once a heater power is set, the heater is lowered to touch the bottom surface, the variance indicator is zeroed, and the heater is returned to a height between 0.2–0.3 mm until an equilibrium temperature is reached. After equilibrium is reached, the heater is lowered by 0.02–0.04 mm, and the gap size is recorded. The lowering of the gap results in a change in the ΔT between the top and bottom of the specimen. After the temperature equilibrates, the system is held at steady state for 15 min. Then, the heater is lowered by 0.02–0.04 mm, and the process is repeated until the gap size reaches ~0.05 mm. This full measurement procedure is repeated multiple times for a range of surrounding furnace temperatures.

3.4. Data collection and analysis

An automated analysis procedure is desirable because it reduces the likelihood of user errors that might arise by manual actions, thereby improving repeatability. The time-dependent probe temperature data are collected and processed post-testing to calculate the thermal conductivity automatically using an analysis script written in Python. The time-dependent thermocouple data for the center thermocouple above and below the specimen are used to calculate the temperature difference. A rolling window mean (RWM) is applied for noise reduction. Because gap changes result in sharp changes to the temperature difference through the specimen, gap changes are automatically detected by comparing the RWM's standard deviation to the difference between the successive smoothed temperature data points. If the difference between two successive datapoints is more than one standard deviation, a gap change is indicated. The time between two gap changes is then used to selectively calculate the time-averaged temperature difference though the specimen while the system is at thermal equilibrium. The thermal resistance at each gap is calculated using the steady state temperaure differences, recorded gap sizes, the power supply's current and voltage, and the heating module's cross sectional area. Then, Eq. (12)—with the appropriate radiation contribution—is fit to the resistance-gap size data using a least-squares trust region reflective algorithm. For Eqs. (13–14) or (16), the integrals are evaluated numerically at each gap size using Simpson's rule.

3.5. Testing materials

Helium gas was purchased from Airgas, Inc., and a commercially available nitrate molten salt heat transfer fluid (MS-1) was purchased from Dynalene, Inc. Helium gas has a well characterized thermal conductivity, and the salt is a relevant high-temperature heat transfer fluid that has relatively low thermal conductivity uncertainties. The MS-1 molten salt is a mixture of $NaNO_3$ and KNO_3 with a documented melting point of 225 °C, though the exact composition is not provided by the supplier. This melting point is 3 °C higher than the minimum melting point of 222 °C suggested by Bauer et al. [101], which corresponds to a 50–50 mol% mixture. This suggests that the mixture could be ±5 mol% off the eutectic point using the phase diagram calculated by the FTSalt FactSage database [102]. However, the thermal conductivity is not expected to vary significantly in this relatively small range [103]. About 40 g of the molten salt was dried under vacuum at 200 °C for ~12 h before loading into the device. The system was filled with helium gas by evacuating the chamber and backfilling it with helium three times at room temperature to ensure that the fill gas did not have any impurities.

3.5.1. Radiative heat transfer in materials

Helium gas is not expected to emit or absorb thermal radiation at the temperatures considered here; therefore, Eq. (11) was used for analysis. For molten salts, the analysis, Eq. (13), requires optical properties that are generally not available in infrared wavelengths. However, Tetreault-Friend et al. studied the absorption coefficient of a similar nitrate mixture of KNO_3–-$NaNO_3$ (40–60 mol%) over 400–2500 nm wavelengths and calculated the re-emission weighted absorption coefficient to be 3706.9 m^{-1} [92]. Even for lengths of 0.1–0.3 mm, the salt should be considered a participating medium Eqs. (12) and (13). There was a weak dependence in temperature reported by Tetreault-Friend et al. [92]; therefore, a discrete value was used for the absorption coefficient.

A mean refractive index value was used for radiative heat transfer adjustments. The mean refractive index was calculated based on application of the Lorentz-Lorenz equation to experimental measurements of refractive index for molten KNO_3 and $NaNO_3$ in Jindal and Harrington [104]. Averaged over the temperature range considered in this study, the mean refractive index of KNO_3–$NaNO_3$ (50–50 mol%) is 1.41. Although the exact

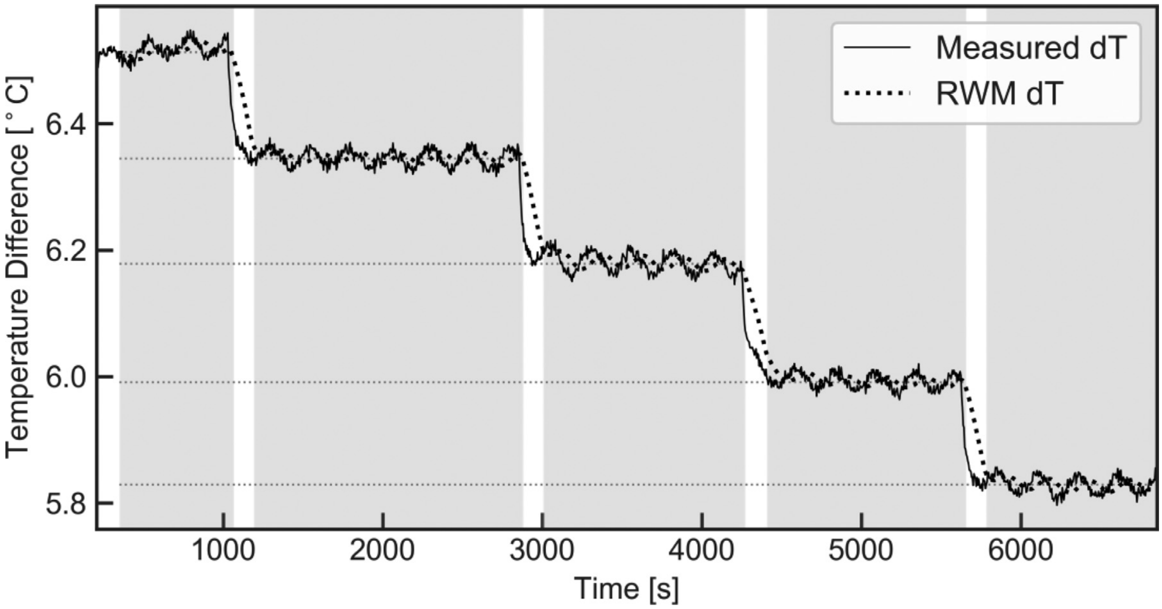

Fig. 5. The measured temperature difference (denoted dT) between the probes for KNO_3–$NaNO_3$ with RWM calculated mean temperature. Shaded regions depict the calculated equilibrium regions.

composition of the MS-1 fluid is unknown, the refractive index of KNO_3–$NaNO_3$ changes negligibly over the range of 45–55 mol% and 55–45 mol% (0.07%). Note that the refractive index only changes by ~2% over this temperature range, justifying the use of a temperature average. Also note that the refractive index measurements Jindal and Harrington [104] were taken at 0.589 µm, but the peak wavelength range of blackbody radiation is 3.74–5.05 µm for the temperatures considered in this study. Unfortunately, short- to mid-wavelength infrared refractive index measurements of molten KNO_3 and $NaNO_3$ (or any molten salt for that matter) have not been taken. With knowledge of a collection of measurements of short- to mid-wavelength infrared refractive index for salts at room temperature [105,106], it is likely that assumed mean refractive index of KNO_3–$NaNO_3$ (50–50 mol%) in this study is an over-approximation because refractive index tends to decrease as a function of wavelength per Cauchy's transmission equation. However, it is unlikely that the error associated with this over-approximation is greater than 10% for this extended wavelength range.

4. Results and discussion

The same system was tested from 300 to 500 °C on helium and the KNO_3–$NaNO_3$ salt. The time-dependent temperature differences though the gap, which were analyzed using the techniques discussed in Section 3.4, during downward gap changes are shown in Fig. 5 for a KNO_3–$NaNO_3$ at 400 °C. A series of gap reductions results in a descending step-change response because the reduction in specimen thickness lowers the thermal resistance between the top and bottom probes. Two to three sets of measurements were taken at each equilibrium temperature to record multiple measurements of the thermal conductivity at a given temperature. Sinusoidal patterns can also be observed in the temperature signal. These patterns corresponded to the surrounding furnace cycling.

The calculated thermal resistance with the curve fits for helium and KNO_3–$NaNO_3$ at 400 and 500 °C are shown in Fig. 6. The thermal resistance for helium is nearly linear with respect to gap size at 400 °C, which is expected since κ_r is independent of gap size. The measurement uncertainties for the helium thermal resistance data were between 6.4 and 7.5%. For helium, the near-linear thermal resistance curves also suggest that convection, which is expected to cause a decreasing slope with respect to increasing gap size, was effectively eliminated. Apparent curvature is observed in the KNO_3–$NaNO_3$ thermal resistance data shown here, especially at 500 °C. However, this trend was not consistent between subsequent runs at any temperature and is statistically significant given that the measurement uncertainty was between 6.8 and 7.9% for the KNO_3–$NaNO_3$ measurements.

The most notable observation is that the relative errors between measured and expected thermal conductivity for both helium and KNO_3–$NaNO_3$ have relatively sharp increases for the results at 500 °C, relative to the lower temperatures. This indicates that systematic errors have biased the measurements, since the thermal conductivity of either materials is expected to have a linear dependence with temperature. The sources of these errors are considered for each material in the following sections.

4.1. Helium results

The average relative error between the known thermal conductivity of helium and the measured values at 300, 400, and 500 °C are 10.5, 13.3, and 17.1%, respectively. The relative error has an increasing trend with temperature. The commonly considered causes of errors in steady-state thermal conductivity measurements include (1) convection, (2) radiative losses, or (3) heat losses, which are all considered to be more likely at higher temperatures. Considering convection first, with a top-heated, parallel plate geometry, there is no correction (empirical or analytical) for quantifying the convection contribution to the effective thermal conductivity. Therefore, the *Ra* number was calculated using the experimental conditions discussed in Section 2. The material properties of helium were taken from the NIST Chemistry WebBook [107]. For these tests, helium had very low *Ra* numbers (<1), so convection had an insignificant role in heat transfer. Considering radiative errors, an under-estimation of the surface emissivity would result in a higher measured conductivity. However, even with a conservatively high emissivity of 0.8, the measured emissivity results in a 5% reduction in the computed thermal conductivity at 500 °C. Therefore, radiative heat transfer alone will not be signifi-

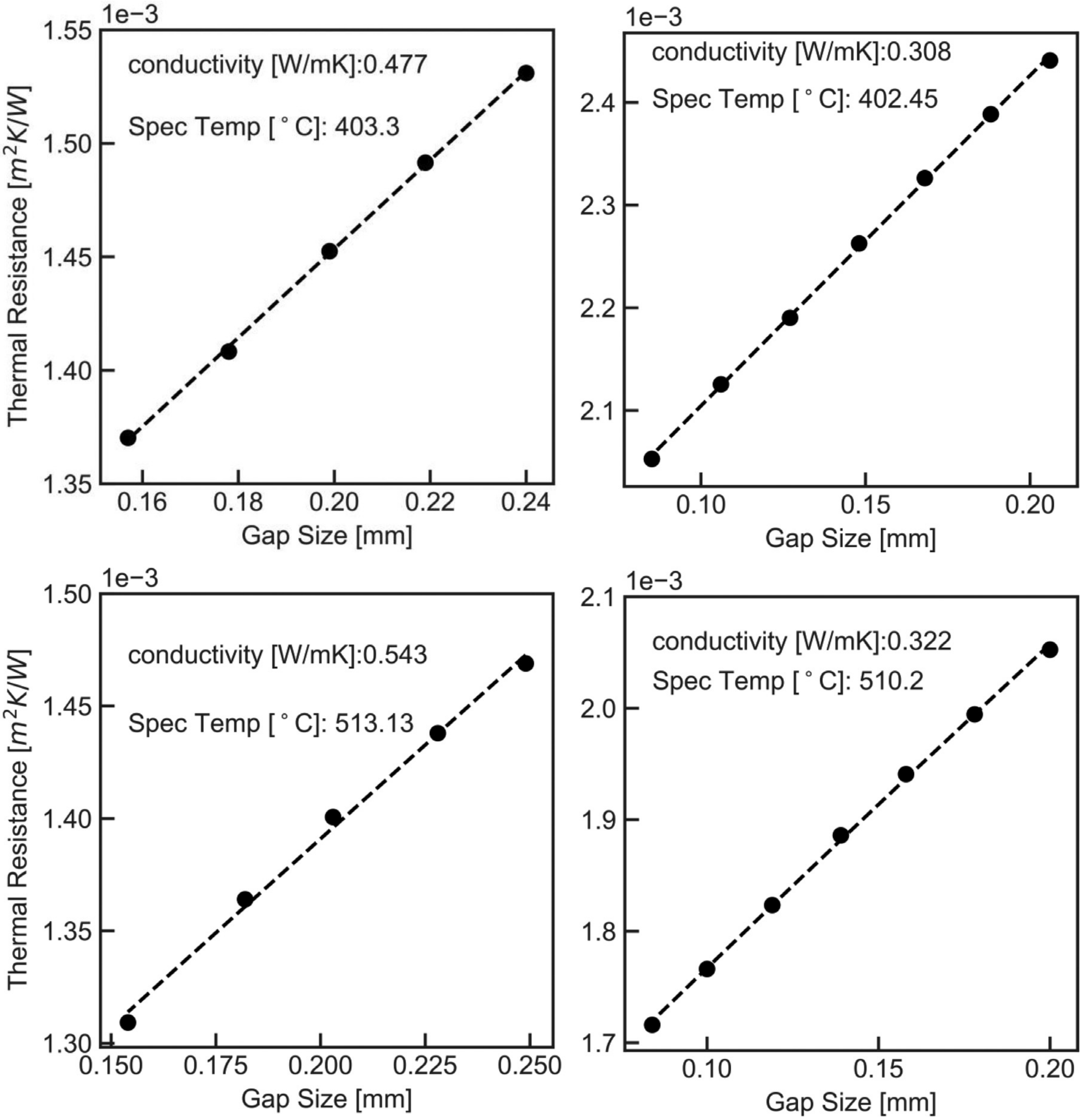

Fig. 6. Examples of the measured thermal resistance for KNO_3–$NaNO_3$ (left) and *He* (right) at 400 °C (top) and 500 °C(bottom) (●) with Eq. (12) fit of thermal resistance (–).

cant enough to cause the relative errors for helium. The last possibility could be heat loss errors.

Nearly all parallel plate thermal conductivity systems employ guard heating to mitigate errant heat losses [82,83,86]. It is reasonable to propose that heat loss axially, either from convection or conduction from the top of the heating source to the top of the internal containment, could result in the errors observed in the test described herein. The experiment containment used in this work is inserted into a tube furnace, but the top flanges are exposed to room temperature air during operation. As such, convection currents within the internal containment (above the gap region) and heat conduction through the structure would be a reasonable expectation. Conduction losses are discussed further in the following section. These loses would be larger at higher temperature because of the increasing temperature difference between the inside of the furnace and the ambient environment. Lower thermal conductivity fluids also result in comparatively higher thermal resistance, which may explain why larger relative errors were observed for the helium tests compared to the KNO_3–$NaNO_3$.

4.2. KNO_3–$NaNO_3$ results

The experimental results from Tufeu et al. [71] and Omotani et al. [108] are shown in Fig. 7. Those authors measured the thermal conductivity of 50–50 mol% KNO_3–$NaNO_3$ using coaxial cylinder and THW, respectively. From 300 to 400 °C, the measured results with the variable gap system show reasonable agreement with the previous measurements from Tufeu et al. [71] and Omotani et al. [108]. The thermal conductivity at 500 °C shows a relatively sharp increase (jump) with temperature. However, extrapolation of the previous thermal conductivity measurement results suggest a slight negative trend [71,108], which also agrees with the theory that molten salts are simple liquids and will therefore have negative temperature dependence [35,38,39]. Furthermore, review of the pure component thermal conductivity [34] recommended data from these techniques, coaxial cylinder [71], and THW [108,109] as primary data. Like the helium tests, these results also show the largest relative errors at 500 °C, which could be caused by convection, radiation, or heat losses.

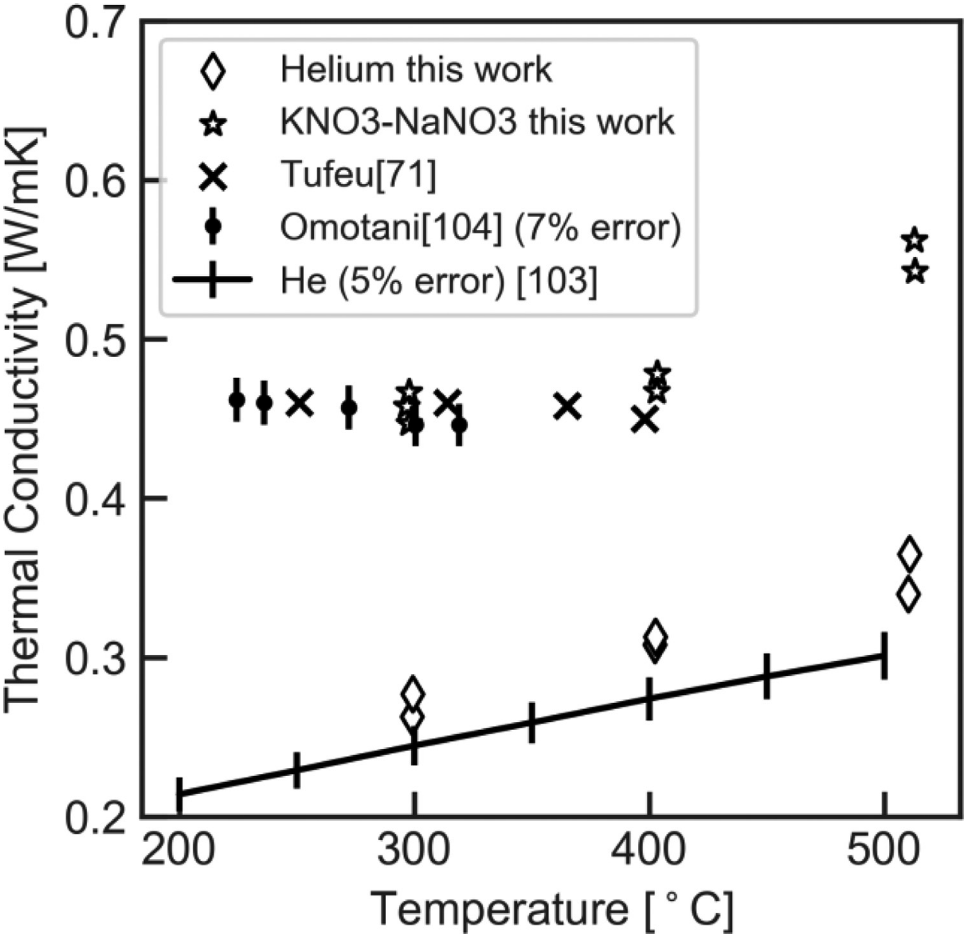

Fig. 7. The measured thermal conductivity of KNO_3–$NaNO_3$ and helium, with helium reference, (–) with 5% error bars [107]; helium measured values (◇); 50–50mol% KNO_3–$NaNO_3$ Tufeu et al., (×) [71]; 50–50mol% KNO_3–$NaNO_3$ Omotani et al., (•) with 7% error bars [108]; and KNO_3–$NaNO_3$ measured values (☆).

Table 1
Thermophysical Properties of 50–50 mol% KNO_3–$NaNO_3$.

Property	Equation (T[°C])	Reference
ρ [g/cm^3]	$2.32 - (7.25 * 10^{-4})T$	[110]
Cp [J/KgK]	1574	[111–114]
κ [W/mK]	$0.472 - (5.65 * 10^{-5})T$	[71,108]
η [mPa s]	$0.074755 * \exp(17, 878.53111/RT)$ [a]	[115]

[a] R is the gas constant

The convection was also considered using analysis of the *Ra* number under the experimental condition. The properties used to calculate the *Ra* number for a 50–50 mol% mixture of KNO_3–$NaNO_3$ were taken from the literature. The density was calculated using the rule of volumetric additivity using the pure component densities recommended in Bauer et al. [110]. The heat capacity was calculated using the basic additivity rule with averaged data from literature [111–114]. The viscosity was calculated using the correlation suggested by Murgulescu et al. [115]. The thermal conductivity was calculated using a linear fit to the data from Omotani et al. [108] and Tufeu et al. [71], extrapolated to higher temperatures. The temperature-dependent equations for the properties of the 50–50 mol% nitrate mixture are shown in Table 1. A contour plot of the calculated *Ra* number with respect to temperature and gap thickness for a specimen with an 8 °C difference through the specimen (the maximum value observed for all cases) is shown in Fig. 8.

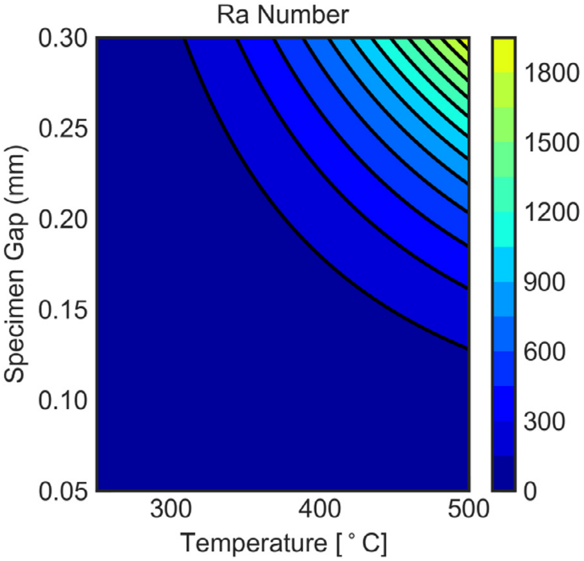

Fig. 8. The calculated *Ra* number for 50–50 mol% KNO_3–$NaNO_3$ with respect to gap size and temperature for 8 °C temperature difference.

The maximum gap size over all tests was 0.3 mm, resulting in *Ra* = 1933 at 500 °C. The *Ra* criterion of 1701 considers a bottom heated arrangement and is therefore a conservative estimate because the top heating arrangement applied in this work will re-

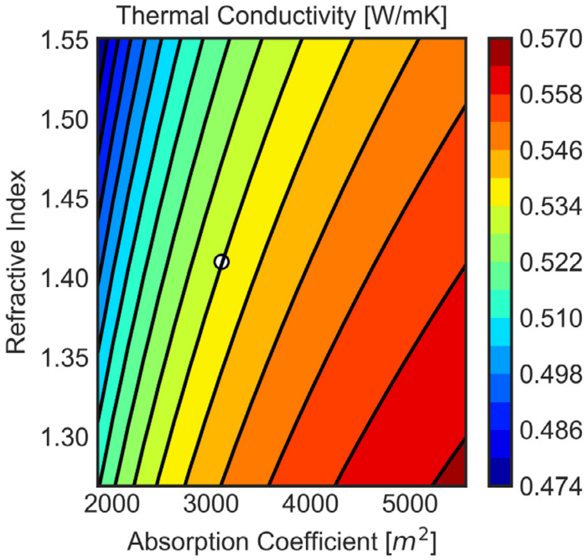

Fig. 9. The calculated thermal conductivity with varying refractive index and absorption coefficient for a test at 500 °C with the estimated values (○).

sist buoyancy-driven flows. However, it was considered necessary to rule out any potential bias from convection. Data points that resulted in an *Ra* number greater than 1700 were omitted. Note that the omission of these few points did not noticeably impact the measured thermal conductivity. The effects of convection would also manifest in the thermal resistance data (Fig. 6) with a non-linear function with respect to gap size. If convection were occurring, an increasing gap size would result in higher convective heat flux. As a result, the thermal resistance results would show a decreasing slope of thermal resistance with respect to increasing gap size, which was not observed in any set of data. Therefore, convection is not expected to be a significant source of error or contribute to the measured increase in conductivity with temperature.

Another source of error could be radiative heat transfer, but it is not expected to be significant enough to result in the magnitude of errors observed at 500 °C. The optical properties are not well understood for nitrate salts at high temperatures in the infrared wavelength range. However, participating behavior, which is expected for this salt, results in the largest contribution of radiative heat transfer. Considering optically thick behavior, no correction for radiative heat transfer is used, which would result in a higher measure of thermal conductivity. From Eq. (11), transparent corrections result in lower calculated conductivities relative to the optically thick case. However, these corrections still result in higher calculated conductivity when compared to the participating case. Therefore, the participating case was further analyzed to investigate whether errors in the estimated *n* or *k* could result in the apparent error at 500 °C.

Fig. 9 shows the calculated thermal conductivity for one of the tests at 500 °C with 10% error on the refractive index and 50% uncertainty on the absorption coefficient. The results show that an overestimation of the absorption coefficient and/or underestimation of the refractive index would result in a higher calculated thermal conductivity. These results show that it is feasible that radiative heat transfer could cause the errors at higher temperature if the estimated optical properties were significantly different. Even with 10% and 50% error on the refractive index and absorption coefficient, respectively, the results would still be above values extrapolated from previous experimental works. It should be also noted that the estimated refractive index is likely an overapproximation (Section 3.5). Given the agreement of results at lower temperatures, this would also imply that either the optical properties change significantly with temperature, which is not expected, or that the lower temperature results are lower than what was previously reported in literature. It is also noted that the radiative conductivity is proportional the gap. Like convection, significant radiative contributions would result in a non-linear function of thermal resistance with respect to gap size, which was not observed. Therefore, radiative heat transfer could contribute to the rise in measured thermal conductivity with temperature, but it is likely not significant enough to be the primary cause. Nonetheless, this work highlights the importance of optical properties, especially when studying participating fluids such as molten salts. These properties will be even more important when examining higher temperature systems such as fluoride and chloride molten salts.

The final cause for a large increase in relative error at 500 °C could be axial heat losses. This is suggested as the most likely cause of error after considering several observations: 1) The errors increased with increasing temperatures, 2) the errors were higher for the more insulating material (helium relative to KNO_3–$NaNO_3$), 3) guard heating was not implemented, 4) linearity in thermal resistance with respect to gap size was observed for all measurements, and 5) the temperature at the resistive heater was higher than the furnace temperature by around 15 °C.

As discussed in Section 4.1, higher furnace and heater temperatures would result in larger temperature differences from the heating module to the top of the experiment and surrounding environment. Therefore, the magnitude of heat losses by conduction through the structure could be expected to increase with increasing operating temperature. This trend was observed in both the helium and molten salt results. Since helium is a more insulating material than the molten salt, downward heat flow through the specimen has a larger thermal resistance. This could explain the larger relative errors for the helium at 300 and 400 °C compared to the molten salt.

Guard heating is a technique where the heat flux from the primary resistive heater is forced to flow downwards, through the specimen. This is done by adding an additional resistive heater (guard heater) above the primary heater. Matching the temperature at the guard heater to the temperature at the primary heater, heat flux in the upward direction is mitigated. This method is also widely applied in similar instruments [86]. Given the lack of guard heating, the current design would be unable to mitigate errant heat losses at temperatures above 400 °C. Therefore, guard heating should be considered for future versions of this technique.

Similarly, the heat flux could “leak” around the specimen, i.e. radially from the heating module to the external containment and downward through the structure of the external containment. This behavior could be considered by adding another thermal resistor in parallel to the specimen’s thermal resistance. With this arrangement, a non-linear response of thermal resistance with respect to gap size would be observed in the measurements, which was not the case for any set of data. On the other hand, axial heat loss upward through the structure, would be treated as a thermal resistor in series with the specimen with heat flux directed away from the heating module. In this case, the linearity of resistance would not be able to indicate significant axial heat losses.

The instrumentation in the design presented herein was not sufficient to quantify potential axial heat losses. Though, heat losses could be estimated considering the heat flow from the heating module, upwards to the rest of the internal containment. For the helium and KNO_3–$NaNO_3$ tests near 500 °C, the average temperature of the heating module and the furnace internal temperature were ~515 °C ~500 °C, respectively. If it is assumed that the center flange on the internal containment (between the heating module and the bellows) has a temperature which is close to the furnace temperature, the heat loss via conduction, upwards through the internal containment would be greater than 40% of the total heat applied to the heating module. This results in a lower heat flux applied to the top of the specimen than what is anticipated, which could account for the magnitude of errors observed in the present measurements. Furthermore, these losses would be expected to increase with increasing system operating temperature. While these noted observations are not conclusive evidence that heat losses influenced the results, suggest that conductive heat loss is a plausible source of the measurement errors.

5. Conclusions

The variable gap system described herein is a versatile tool for characterization of steady-state heat transfer in high-temperature fluids that are desirable for next-generation energy systems. A system was designed and built that can accommodate a variety of corrosive fluids in a controlled environment up to 500 °C. Measurement in the steady-state regime with the variable gap technique allows for a direct measurement of thermal conductivity and circumvents the need to correct for thermal resistance arising from contact and barrier materials. The working equations and data analysis account for multiple types of thermal radiative interactions, which will be essential for measurement at more extreme temperatures. The testing results with He and KNO_3–$NaNO_3$ were presented with corrections for radiative heat transfer at temperatures from 300 to 500 °C. These results showed agreement with literature values at 300 and 400 °C but had relatively large errors at 500 °C. Consideration of the results suggested that axial heat loss could be a major source of error, yet the values are still reasonably close, considering the uncertainties of previous fluid thermal measurements [34]. The addition of guard heating will be necessary before accurate measurements at higher temperatures can be taken. This work highlights the capability of the variable gap technique for analyzing the thermal conductivity of high-temperature fluids which will be essential for providing data supporting the development of many advanced energy systems.

Declaration of Competing Interest

The authors declare the following financial interests/personal relationships which may be considered as potential competing interests: Ryan C. Gallagher reports financial support was provided by US Department of Energy. Ryan C. Gallagher has a patent pending to Oak Ridge National Laboratory.

CRediT authorship contribution statement

Ryan C. Gallagher: Conceptualization, Methodology, Validation, Software, Formal analysis, Investigation, Resources, Data curation, Writing – original draft, Visualization. **Anthony Birri:** Investigation, Data curation, Writing – review & editing. **Nick Russell:** Formal analysis, Software, Resources, Data curation. **N. Dianne B. Ezell:** Conceptualization, Writing – review & editing, Project administration.

Acknowledgements

This work was supported by the Department of Energy's Office of Nuclear Energy Advanced Reactor Technologies program's Molten Salt Reactor Campaign. This work was facilitated and performed at Oak Ridge National Laboratory. The authors would also like to acknowledge Shay Chapel for his role in the mechanical design, Kevin Robb for review of the manuscript and technical discussions on molten salt systems, and Lei R. Cao at Ohio State University for his advisory support to the primary, corresponding author.

References

[1] P.D. Myers Jr, D.Y Goswami, Thermal energy storage using chloride salts and their eutectics, Appl. Therm. Eng. 109 (2016) 889–900.

[2] K. Vignarooban, X. Xu, A. Arvay, K. Hsu, A.M. Kannan, Heat transfer fluids for concentrating solar power systems–a review, Appl. Energy 146 (2015) 383–396.

[3] A.G. Fernández, et al., Mainstreaming commercial CSP systems: a technology review, Renew. Energy 140 (2019) 152–176.

[4] E. González-Roubaud, D. Pérez-Osorio, C. Prieto, Review of commercial thermal energy storage in concentrated solar power plants: steam vs. molten salts, Renew. Sustain. Energy Rev. 80 (2017) 133–148.

[5] L.A. Weinstein, et al., Concentrating solar power, Chem. Rev. 115 (2015) 12797–12838.

[6] U. Pelay, L. Luo, Y. Fan, D. Stitou, M. Rood, Thermal energy storage systems for concentrated solar power plants, Renew. Sustain. Energy Rev. 79 (2017) 82–100.

[7] P. Gauché, et al., System value and progress of CSP, Solar Energy 152 (2017) 106–139.

[8] A. Bonk, S. Sau, N. Uranga, M. Hernaiz, T. Bauer, Advanced heat transfer fluids for direct molten salt line-focusing CSP plants, Prog. Energy Combust. Sci. 67 (2018) 69–87.

[9] M. Mehos, et al., Concentrating Solar Power Gen3 Demonstration Roadmap, National Renewable Energy Lab.(NREL, Golden, CO (United States), 2017 Report No. NREL/TP-5500-67464.

[10] M. Liu, et al., Review on concentrating solar power plants and new developments in high temperature thermal energy storage technologies, Renew. Sustain. Energy Rev. 53 (2016) 1411–1432.

[11] B.D. Iverson, T.M. Conboy, J.J. Pasch, A.M. Kruizenga, Supercritical CO_2 Brayton cycles for solar-thermal energy, Appl Energy 111 (2013) 957–970.

[12] M.M. Kenisarin, High-temperature phase change materials for thermal energy storage, Renew. Sustain. Energy Rev. 14 (2010) 955–970.

[13] G. Alva, Y. Lin, G. Fang, An overview of thermal energy storage systems, Energy 144 (2018) 341–378.

[14] S. Khare, M. Dell'Amico, C. Knight, S. McGarry, Selection of materials for high temperature latent heat energy storage, Sol. Energy Mater. Sol. Cells 107 (2012) 20–27.

[15] B. Mignacca, G. Locatelli, Economics and finance of Molten Salt Reactors, Progress Nucl. Energy 129 (2020) 103503.

[16] C.W. Forsberg, P.F. Peterson, P.S. Pickard, Molten-salt-cooled advanced high--temperature reactor for production of hydrogen and electricity, Nucl. Technol. 144 (2003) 289–302.

[17] Y.-l.H. Kun Wang, Thermodynamic analysis and optimization of a molten salt solar power tower integrated with a recompression supercritical CO_2 Brayton cycle based on integrated modeling, Energy Conver. Manage. 135 (2017) 336–350, doi:10.1016/j.enconman.2016.12.085.

[18] J. Serp, et al., The molten salt reactor (MSR) in generation IV: overview and perspectives, Progress Nucl. Energy 77 (2014) 308–319.

[19] K. Aoto, et al., A summary of sodium-cooled fast reactor development, Progress Nucl. Energy 77 (2014) 247–265.

[20] A.C. Kadak, The status of the US high-temperature gas reactors, Engineering 2 (2016) 119–123.

[21] F.L. Tabarés, Present status of liquid metal research for a fusion reactor, Plasma Phys. Controlled Fusion 58 (2015) 014014.

[22] F. Tabarés, et al., Reactor plasma facing component designs based on liquid metal concepts supported in porous systems, Nucl. Fusion 57 (2016) 016029.

[23] C. Forsberg, G. Zheng, R.G. Ballinger, S.T. Lam, Fusion blankets and fluoride-salt-Cooled high-temperature reactors with flibe salt coolant: common challenges, tritium control, and opportunities for synergistic development strategies between fission, fusion, and solar salt technologies, Nucl. Technol. 206 (2020) 1778–1801.

[24] J.W. McMurray, Multi-Physics Simulations for Molten Salt Reactor Evaluation: Chemistry Modeling and Database Development, Oak Ridge National Laboratory, 2018 Report No. ORNL/SPR-2018/864.

[25] J.W. Mcmurray, et al., Roadmap For Thermal Property Measurements of Molten Salt Reactor systems, Oak Ridge National Lab.(ORNL), Oak Ridge, TN (United States), 2021 Report No. ORNL/SPR-2020/1865.

[26] Y. Tao, Y.-L. He, A review of phase change material and performance enhancement method for latent heat storage system, Renew. Sustain. Energy Rev. 93 (2018) 245–259.

[27] J.-H.C. Xue-Hui An, Tao Su, Peng Zhang, Determination pf thermal physical properties of alkali flouride/carbonate eutectic molten salt, AIP Conf. Proc. 1850 (2017), doi:10.1063/1.4984415.

[28] H. Tiznobaik, D. Shin, Enhanced specific heat capacity of high-temperature molten salt-based nanofluids, Int. J. Heat Mass Transf. 57 (2013) 542–548.

[29] A. Kasaeian, A.T. Eshghi, M. Sameti, A review on the applications of nanofluids in solar energy systems, Renew. Sustain. Energy Rev. 43 (2015) 584–598.

[30] V.M. Nunes, M.J. Lourenço, F.J. Santos, C.A. Nieto de Castro, Importance of accurate data on viscosity and thermal conductivity in molten salts applications, J. Chemical Eng. Data 48 (2003) 446–450.

[31] A. Palacios, L. Cong, M. Navarro, Y. Ding, C. Barreneche, Thermal conductivity measurement techniques for characterizing thermal energy storage materials–A review, Renew. Sustain. Energy Rev. 108 (2019) 32–52.

[32] D.F. Williams, L.M. Toth, K.T. Clarno, Assessment of Candidate Molten Salt Coolants For the Advanced High-Temperature Reactor (AHTR), Oak Ridge National Laboratory, 2006 Report No. ORNL/TM-2006/12.

[33] J. Magnusson, M. Memmott, T. Munro, Review of thermophysical property methods applied to fueled and un-fueled molten salts, Ann. Nucl. Energy 146 (2020) 107608.

[34] C.D. Chliatzou, M.J. Assael, K. Antoniadis, M.L. Huber, W.A. Wakeham, Reference correlations for the thermal conductivity of 13 inorganic molten salts, J. Phys. Chem. Ref. Data 47 (2018) 033104.

[35] A.E. Gheribi, J.A. Torres, P. Chartrand, Recommended values for the thermal conductivity of molten salts between the melting and boiling points, Sol. Energy Mater. Sol. Cells 126 (2014) 11–25.

[36] M.Z. Hossain, M.H. Kassaee, S. Jeter, A.S. Teja, A new model for the thermal conductivity of molten salts, Int. J. Thermophys. 35 (2014) 246–255.

[37] Q.-G. Zhao, S.-J. Liu, H. Guo, X. Chen, A theoretical model for predicting the thermal conductivity of binary molten salts, Int. J. Heat Mass Transf. 92 (2016) 639–642.

[38] R. DiGuilio, A.S. Teja, A rough hard-sphere model for the thermal conductivity of molten salts, Int. J. Thermophys. 13 (1992) 855–871.

[39] A.E. Gheribi, P. Chartrand, Thermal conductivity of molten salt mixtures: theoretical model supported by equilibrium molecular dynamics simulations, J. Chem. Phys. 144 (2016) 084506.

[40] A. Gheribi, et al., Prediction of the thermophysical properties of molten salt fast reactor fuel from first-principles, Mol. Phys. 112 (2014) 1305–1312.

[41] N. Galamba, C. Nieto de Castro, J.F. Ely, Thermal conductivity of molten alkali halides from equilibrium molecular dynamics simulations, J. Chem. Phys. 120 (2004) 8676–8682.

[42] M. Salanne, D. Marrocchelli, C. Merlet, N. Ohtori, P.A. Madden, Thermal conductivity of ionic systems from equilibrium molecular dynamics, J. Phys. 23 (2011) 102101.

[43] A.m.E. Gheribi, M. Salanne, P. Chartrand, Formulation of temperature-dependent thermal conductivity of NaF, β-Na_3AlF_6, $Na_5Al_3F_{14}$, and molten Na3AlF6 supported by equilibrium molecular dynamics and density functional theory, J. Phys. Chem. C 120 (2016) 22873–22886.

[44] Z. Rong, J. Ding, W. Wang, G. Pan, S. Liu, Ab-initio molecular dynamics calculation on microstructures and thermophysical properties of $NaCl$–$CaCl_2$–$MgCl_2$ for concentrating solar power, Sol. Energy Mater. Sol. Cells 216 (2020) 110696.

[45] G. Paul, M. Chopkar, I. Manna, P. Das, Techniques for measuring the thermal conductivity of nanofluids: a review, Renew. Sustain. Energy Rev. 14 (2010) 1913–1924.

[46] D. Zhao, X. Qian, X. Gu, S.A. Jajja, R. Yang, Measurement techniques for thermal conductivity and interfacial thermal conductance of bulk and thin film materials, J. Electron. Packag. 138 (2016) 040802.

[47] M.J. Assael, K.D. Antoniadis, W.A. Wakeham, Historical evolution of the transient hot-wire technique, Int. J. Thermophys. 31 (2010) 1051–1072.

[48] C.N. De Castro, J. Calado, W. Wakeham, M. Dix, An apparatus to measure the thermal conductivity of liquids, J. Phys. E 9 (1976) 1073.

[49] Y. Nagasaka, A. Nagashima, Simultaneous measurement of the thermal conductivity and the thermal diffusivity of liquids by the transient hot-wire method, Rev. Sci. Instrum. 52 (1981) 229–232.

[50] Y. Nagasaka, A. Nagashima, Absolute measurement of the thermal conductivity of electrically conducting liquids by the transient hot-wire method, J. Phys. E. 14 (1981) 1435.

[51] M. Assael, E. Charitidou, G. Georgiadis, W. Wakeham, Absolute measurement of the thermal conductivity of electrically conducting liquids, Berichte der Bunsengesellschaft für physikalische Chemie 92 (1988) 627–631.

[52] J.G. Bleazard, A.S. Teja, Thermal conductivity of electrically conducting liquids by the transient hot-wire method, J. Chem. Eng. Data 40 (1995) 732–737.

[53] W. Yu, S.U.-S. Choi, Influence of insulation coating on thermal conductivity measurement by transient hot-wire method, Rev. Sci. Instrum. 77 (2006) 076102.

[54] M. Hoshi, T. Omotani, A. Nagashima, Transient method to measure the thermal conductivity of high-temperature melts using a liquid-metal probe, Rev. Sci. Instrum. 52 (1981) 755–758.

[55] X. Zhang, M. Fujii, Simultaneous measurements of the thermal conductivity and thermal diffusivity of molten salts with a transient short-hot-wire method, Int. J. Thermophys. 21 (2000) 71–84.

[56] S.E. Gustafsson, Transient plane source techniques for thermal conductivity and thermal diffusivity measurements of solid materials, Rev. Sci. Instrum. 62 (1991) 797–804.

[57] M. Piro, K. Lipkina, D. Hallatt, Exploring crucible designs for differential scanning calorimetry measurements of fluoride salts, Thermochim. Acta 699 (2021) 178860.

[58] M. Wingert, A. Zhao, Y. Kodera, S. Obrey, J. Garay, Frequency-domain hot-wire sensor and 3D model for thermal conductivity measurements of reactive and corrosive materials at high temperatures, Rev. Sci. Instrum. 91 (2020) 054904.

[59] A. Harris, S. Kazachenko, R. Bateman, J. Nickerson, M. Emanuel, Measuring the thermal conductivity of heat transfer fluids via the modified transient plane source (MTPS), J. Therm. Anal. Calorim. 116 (2014) 1309–1314.

[60] W. Parker, R. Jenkins, C. Butler, G. Abbott, Flash method of determining thermal diffusivity, heat capacity, and thermal conductivity, J. Appl. Phys. 32 (1961) 1679–1684.

[61] Y. Tada, M. Harada, M. Tanigaki, W. Eguchi, Laser flash method for measuring thermal conductivity of liquids. Application to molten salts, Ind. Eng. Chem. 20 (1981) 333–336.

[62] H. Ohta, G. Ogura, Y. Waseda, M. Suzuki, Thermal diffusivity measurements of molten salts using a three-layered cell by the laser flash method, Rev. Sci. Instrum. 61 (1990) 2645–2649.

[63] X.-H. An, J.-H. Cheng, H.-Q. Yin, L.-D. Xie, P. Zhang, Thermal conductivity of high temperature fluoride molten salt determined by laser flash technique, Int. J. Heat Mass Transf. 90 (2015) 872–877.

[64] K. Sugiura, M. Yamauchi, K. Tanimoto, Y. Yoshitani, Evaluation of volatile behaviour and the volatilization volume of molten salt in DIR-MCFC by using the image measurement technique, J. Power Sources 145 (2005) 199–205.

[65] Y. Grosu, L. Gonzalez-Fernandez, U. Nithiyanantham, A. Faik, Wettability control for correct thermophysical properties determination of molten salts and thier nanofluids, Energies 12 (2019), doi:10.3390/en12193765.

[66] Y. Nagasaka, T. Hatakeyama, M. Okuda, A. Nagashima, Measurement of the thermal diffusivity of liquids by the forced Rayleigh scattering method: theory and experiment, Rev. Sci. Instrum. 59 (1988) 1156–1168.

[67] N. Nakazawa, Y. Nagasaka, A. Nagashima, Experimental determination of the thermal diffusivity of molten alkali halides by the forced Rayleigh scattering method. II. Molten NaBr, KBr, RbBr, and CsBr, Int. J. Thermophys. 13 (1992) 753–762.

[68] Y. Nagasaka, N. Nakazawa, A. Nagashima, Experimental determination of the thermal diffusivity of molten alkali halides by the forced Rayleigh scattering method. I. Molten LiCl, NaCl, KCl, RbCl, and CsCl, Int. J. Thermophys. 13 (1992) 555–574.

[69] N. Nakazawa, Y. Nagasaka, A. Nagashima, Experimental determination of the thermal diffusivity of molten alkali halides by the forced Rayleigh scattering method. III. molten NaI, KI, RbI, and CsI, Int. J. Thermophys. 13 (1992) 763–772.

[70] Y. Nagasaka, A. Nagashima, Corresponding states correlation for the thermal conductivity of molten alkali halides, Int. J. Thermophys. 14 (1993) 923–936.

[71] R. Tufeu, J. Petitet, L. Denielou, B. Le Neindre, Experimental determination of the thermal conductivity of molten pure salts and salt mixtures, Int. J. Thermophys. 6 (1985) 315–330.

[72] V. Golyshev, M. Gonik, High-temperature thermophysical properties of non-scattering semitransparent materials. III: thermal conductivity of melts, High Temperatures. High Pressures 24 (1992) 677–688.

[73] R. Tufeu, B. Le Naindre, Knudsen effect in determining the thermal conductivity of gases by the coaxial-cylinder method, Journal of engineering physics 36 (1979) 318–323.

[74] A.S. Iyengar, A.R. Abramson, Comparative radial heat flow method for thermal conductivity measurement of liquids, J Heat Transfer 131 (2009).

[75] G.W. Todd, Thermal conductivity of air and other gases, Proc. R Soc. London. Series A 83 (1909) 19–39.

[76] U. Hammerschmidt, Thermal conductivity of a wide range of alternative refrigerants measured with an improved guarded hot-plate apparatus, Int. J. Thermophys. 16 (1995) 1203–1211.

[77] A. Challoner, R. Powell, Thermal conductivities of liquids: new determinations for seven liquids and appraisal of existing values, Proc. R Soc. London. Series A 238 (1956) 90–106.

[78] A. Fröba, et al., Thermal conductivity of ionic liquids: measurement and prediction, Int. J. Thermophys. 31 (2010) 2059–2077.

[79] R. Santini, P. Cerisier, J. Pantaloni, L. Tadrist, Measurement of thermal conductivity of molten salts in the range 100-500/sup 0/C, Int. J. Heat Mass Transf. (1984) 27.

[80] H. Poltz, R. Jugel, The thermal conductivity of liquids—IV: temperature dependence of thermal conductivity, Int. J. Heat Mass Transf. 10 (1967) 1075–1088.

[81] R. Braun, S. Fischer, A. Schaber, Elimination of the radiant component of measured liquid thermal conductivities, Wärme-und Stoffübertragung 17 (1983) 121–124.

[82] J. Cooke, Development of the Variable-Gap Technique For Measuring the Thermal Conductivity of Fluoride Salt Mixtures, Oak Ridge National Laboratory, 1973 Report No. ORNL-4831.

[83] J. Cooke, in: Compendium of Thermophysical Property Measurement Methods, Springer, 1992, pp. 201–235.

[84] L. Muhmood, Modeling for thermal conductivity of ternary molten nitrate salts using unit cell concept, Int. J. Thermophys. 41 (2020) 1–12.

[85] K. Yao, et al., Influence of thermal contact resistance on thermal conductivity measurement with a high-temperature guarded hot plate apparatus, Int. J. Thermophys. 41 (2020) 1–12.

[86] M.H. Rausch, K. Krzeminski, A. Leipertz, A.P. Fröba, A new guarded parallel–plate instrument for the measurement of the thermal conductivity of fluids and solids, Int. J. Heat Mass Transf. 58 (2013) 610–618.

[87] R. Viskanta, & R. Grosh. Heat transfer by simultaneous conduction and radiation in an absorbing medium. (1962).

[88] Q. Hao, et al., Nanograined GeSe4 as a Thermal Insulation Material, Front. Energy Res. 21 (2018).

[89] H. Zhang, Y. Li, W. Tao, Effect of radiative heat transfer on determining thermal conductivity of semi-transparent materials using transient plane source method, Appl. Therm. Eng. 114 (2017) 337–345.

[90] V. Schick, et al. in Journal of Physics: Conference Series. 012078 (IOP Publishing).

[91] M. Karim, M. Islam, O. Arthur, P.K. Yarlagadda, Performance of graphite-dispersed Li2CO3-K2CO$_3$ molten salt nanofluid for a direct absorption solar collector system, Molecules 25 (2020) 375.

[92] M. Tetreault-Friend, L.A. Gray, S. Berdibek, T. McKrell, A.H. Slocum, Optical properties of high temperature molten salt mixtures for volumetrically absorbing solar thermal receiver applications, Solar Energy 153 (2017) 238–248.

[93] E.S. Chaleff, T. Blue, P. Sabharwall, Radiation heat transfer in the Molten Salt FLiNaK, Nucl. Technol. 196 (2016) 53–60.

[94] W. Derdeyn, M.A. Dbai, R.O. Scarlat, M. Trujillo, Flibe radiative heat transfer, Trans. Am. Nucl. Soc. 118 (2018).

[95] M. Kohler, Einfluß der Strahlung auf den Wärmetransport durch eine Flüssigkeitsschicht, Zeitschrigt Fur Angewandte Physik 18 (1965) 356.

[96] H. Poltz, Die wärmeleitfähigkeit von flüssigkeiten II: der strahlungsanteil der effektiven wärmeleitfähigkeit, Int. J. Heat Mass Transf. 8 (1965) 515–527.

[97] R. Mostert, H. Van den Berg, P. Van Der Gulik, A guarded parallel-plate instrument for measuring the thermal conductivity of fluids in the critical region, Rev. Sci. Instrum. 60 (1989) 3466–3474.

[98] M. Gitterman, Hydrodynamics of fluids near a critical point, Rev. Mod. Phys. 50 (1978) 85.

[99] S. Taylor, et al., Investigating relationship between surface topography and emissivity of metallic additively manufactured parts, Int. Commun. Heat Mass Transf. 115 (2020) 104614.

[100] C. Davisson, J. Weeks, The relation between the total thermal emissive power of a metal and its electrical resistivity, JOSA 8 (1924) 581–605.

[101] T. Bauer, D. Laing, & R. Tamme, in *Advances in Science and Technology.* 272–277 (Trans Tech Publ).

[102] C.W. Bale, et al., Reprint of: factSage thermochemical software and databases, 2010–2016, Calphad 55 (2016) 1–19.

[103] Q.-G. Zhao, C.-X. Hu, S.-J. Liu, H. Guo, Y.-T. Wu, The thermal conductivity of molten $NaNO_3$, KNO_3, and their mixtures, Energy Procedia 143 (2017) 774–779.

[104] H.R. Jindal, G.W. Harrington, Refractometry in fused alkali nitrates and thiocyanates, J. Phys. Chem. 71 (1967) 1688–1694.

[105] M.R. Querry, *Optical constants of minerals and other materials from the millimeter to the ultraviolet*, Develop. Eng. Center (1987).

[106] M.I. Cotterell, R.E. Willoughby, B.R. Bzdek, A.J. Orr-Ewing, J.P. Reid, A complete parameterisation of the relative humidity and wavelength dependence of the refractive index of hygroscopic inorganic aerosol particles, Atmos. Chem. Phys. 17 (2017) 9837–9851.

[107] E.W. Lemmon, M.O. McLinden, & D.G. Friend, in *NIST Chemistry Webbook, NIST Standard Reference Database Number 69* (eds P.J. Linstrom & W.G. Mallard) (National Institute of Standards and Technology, Gaithersburg MD, 20899).

[108] T. Omotani, Y. Nagasaka, A. Nagashima, Measurement of the thermal conductivity of KNO_3-$NaNO_3$ mixtures using a transient hot-wire method with a liquid metal in a capillary probe, Int. J. Thermophys. 3 (1982) 17–26.

[109] T. Omotani, A. Nagashima, Thermal conductivity of molten salts, HTS and the lithium nitrate-sodium nitrate system, using a modified transient hot-wire method, J. Chem. Eng. Data 29 (1984) 1–3.

[110] T. Bauer, A. Bonk, Semi-empirical density estimations for binary, ternary and multicomponent alkali nitrate–nitrite molten salt mixtures, Int. J. Thermophys. 39 (2018) 1–26.

[111] R.W. Carling, Heat capacities of $NaNO_3$ and KNO_3 from 350 to 800K, Thermochim. Acta 60 (1983) 265–275.

[112] D.J. Rogers, G.J. Janz, Melting-crystallization and premelting properties of sodium nitrate-potassium nitrate. Enthalpies and heat capacities, J. Chem. Eng. Data 27 (1982) 424–428.

[113] K. Ichikawa, T. Matsumoto, The heat capacities of lithium, sodium, potassium, rubidium, and caesium nitrates in the solid and liquid states, Bull. Chem. Soc. Jpn. 56 (1983) 2093–2100.

[114] Y. Takahashi, R. Sakamoto, M. Kamimoto, Heat capacities and latent heats of $LiNO_3$, $NaNO_3$, and KNO_3, Int. J. Thermophys. 9 (1988) 1081–1090.

[115] I. Murgulescu, S. Zuca, Viscosity of binary mixtures of molten nitrates as a function of ionic radius—II, Electrochim. Acta 14 (1969) 519–526.